Title

Simulations of CO2 injection into fractures and faults for improving their geophysical characterization at EGS sites

Authors

Borgia, Andrea
Oldenburg, Curtis M
Zhang, Rui
et al.

Publication Date

2017-09-01

DOI

10.1016/j.geothermics.2017.05.002

Peer reviewed

Simulations of CO_2 injection into fractures and faults for improving their geophysical characterization at EGS sites

Author links open overlay panel[AndreaBorgia[a]](#)[Curtis M.Oldenburg[a]](#)[RuiZhang[b]](#)[LehuaPan[a]](#)[Thomas M.Daley[a]](#)[StefanFinsterle[a]](#)[T.S.Ramakrishnan[c]](#)
Show more

https://doi.org/10.1016/j.geothermics.2017.05.002Get rights and content

Highlights

- We inject supercritical CO_2 into fractures for improving fault characterization.
- Supercritical CO_2 enters only the fractures, being excluded from the matrix.
- Supercritical CO_2 in fractures creates measurable changes in seismic velocities.
- Push-pull tests allow a characterization of hydrogeologic properties of fractures.

Abstract

We propose the use of CO_2 in push-pull well tests to improve geophysical identification and characterization of fractures and faults at enhanced geothermal system (EGS) sites. Using TOUGH2/ECO2N, we carried out numerical experiments of push-pull injection-production cycling of CO_2 into idealized vertical fractures and faults to produce pressure-saturation-temperature conditions that can be analyzed for their geophysical response. Our results show that there is a strong difference between injection and production mainly because of CO_2 buoyancy. While the CO_2-plume grows laterally and upward during injection, not all CO_2 is recovered during the subsequent production phase. Even under the best conditions for recovery, at least 10% of the volume of the pores still remains filled with CO_2. To improve EGS characterization, comparisons can be made of active seismic methods carried out before and after (time lapse mode) CO_2 injection into the fracture or fault. We find that across the CO_2 saturation range, C_{11} (the normal stiffness in the horizontal direction perpendicular to the fracture plane) varies between maximum and minimum values by about 15%. It reaches a maximum at around 6% gas saturation, decreasing exponentially to a minimum at higher saturations. Our results suggest that CO_2 injection can be effectively used to infiltrate fault and

fracture zones reaching about optimal saturation values in order to enhance seismic imaging at EGS sites.

Keywords

CO_2 injection
Faults characterization
Faults imaging
Seismic imaging
EGS

1. Introduction

For sustainable geothermal energy production, fracture permeability is essential to provide both rock-fluid surfaces for adequate heat transfer and sufficient fluid production rates. In most geothermal fields, a small number of extensive fractures and faults dominate fluid production. At enhanced geothermal system (EGS) sites, stimulation is used to create a more pervasive network of fractures to access more efficiently the heat stored in the volume of hot rock (Genter et al., 2010).

In order to design and evaluate reservoir development and stimulation strategies, effective fracture and fault network characterization of both natural and stimulated reservoirs is essential. To achieve this characterization, we propose to do active-source geophysical monitoring and well logging, and use CO_2 in push-pull well testing to enhance the contrast in geophysical properties between fractures and matrix and thereby improve fracture characterization (Borgia et al., 2015, Oldenburg et al., 2016). The flow and transport properties of supercritical CO_2 relevant to its use in brightening faults and fractures for active seismic (or well-logging) imaging are:

1) CO_2 is much more compressible than water at EGS conditions, creating significant variations in stiffness tensor and correspondingly in seismic velocity;

2) CO_2 is non-wetting and will therefore tend to stay in the fault/fracture and resist flowing into fine-grained matrix; and

3) CO_2 is less viscous than ambient brine at geothermal conditions, facilitating fracture/fault permeation.

Although supercritical CO_2 has gas-like viscosity, which enhances its mobility, it is quite dense relative to other gases like nitrogen, which is an advantage for decreasing the negative consequences of strong buoyant rise in vertical faults and fractures.
In this paper, we report on simulated push-pull injection-production cycling of CO_2 into single fractures and faults to produce pressure-saturation-temperature conditions that can be analyzed for their geophysical and wellbore logging response.

2. Conceptual model

Faults and fractures may be conceptualized using five independent topologies (Fig. 1), which serve to define basic model geometries. While these end-member topologies may only grossly represent the details and complexity of fractures and faults in an actual geothermal field, and their relations to true tectonic stresses, they are useful abstractions to understand fundamental behaviors that will be observed in natural systems.

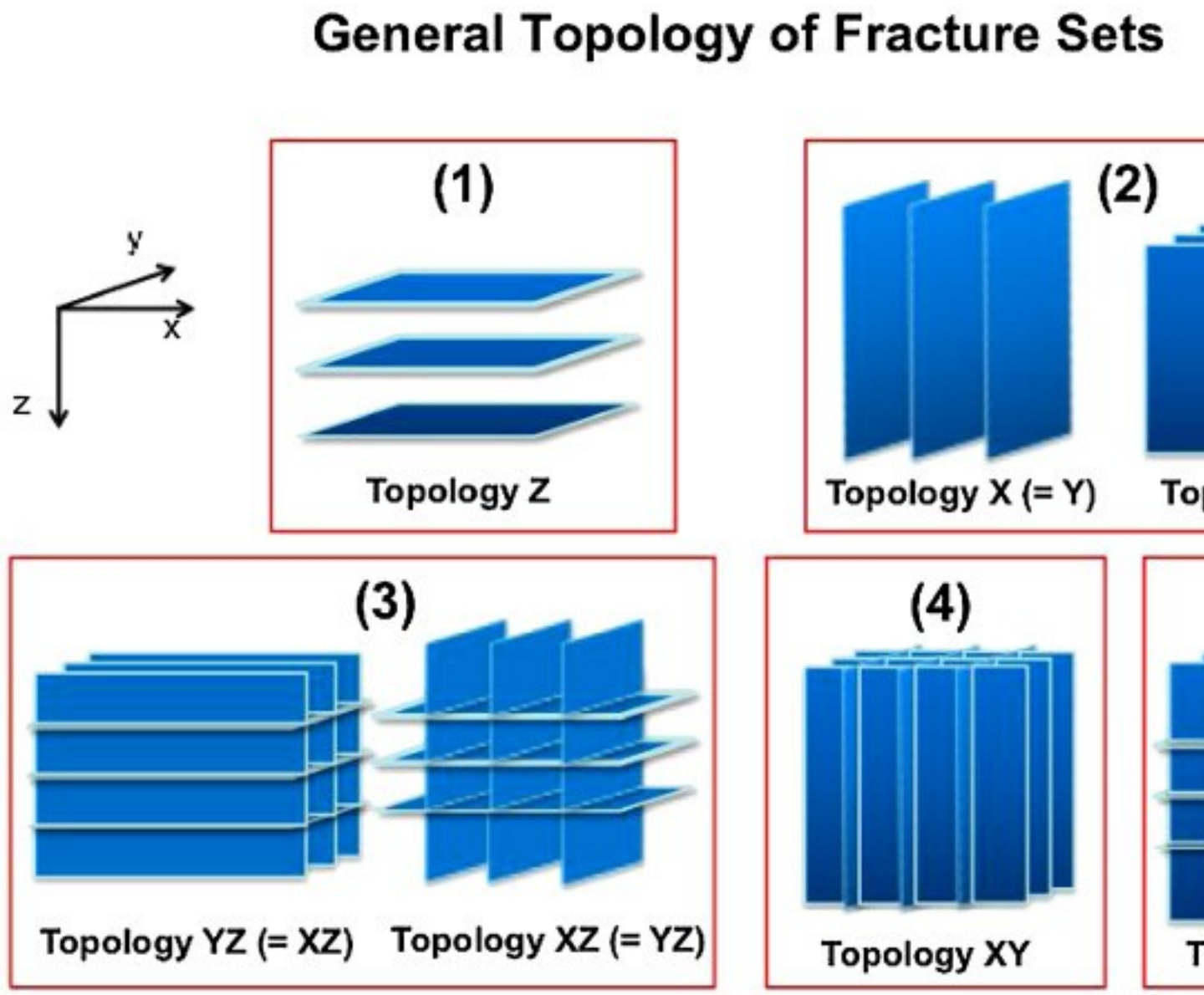

1. Download high-res image (854KB)
2. Download full-size image

Fig. 1. The five independent fracture topologies. See text for explanation.

Unconnected horizontal faults and fractures belong to Topology 1 where horizontal faults and fractures are perpendicular to the z-axis (which is here assumed vertical). Topology 2 occurs when vertical faults and fractures are perpendicular either to the x or y spatial directions. As the faults and fractures in one of these two topologies become more and more interconnected, the other topologies emerge. If vertical or horizontal parallel fault and fractures become fully connected in the horizontal or vertical directions, respectively, Topology 3 occurs. Topology 4 develops if there are two sets of vertical faults and fractures. Topology 5 includes three sets of fault and fractures, each

perpendicular to one of the main axes. In the real world, a set of faults and fractures is rarely perpendicular to any different set of faults and fractures. However, we can deform our reference coordinate system so that each fracture set is actually perpendicular to one of the major axes. This implies that topology reference axes do not need to be orthogonal, nor horizontal or vertical. The ranges of fracture and fault system dimensions occurring in nature are indicated in Table 1.

Table 1. Characteristic fracture geometry and ranges used in our modeling studies. See Fig. 2 for symbol definitions.

		min	max
A = fracture aperture		10^{-5}	10^{-4} (m)
d = damage zone thickness		10^{-1}	10^{1} (m)
S = fracture spacing		1	10^{2} (m)
D = fracture density	=1/S	1	10^{-2} (fracture/m)
H = fracture zone thickness		1	10^{3} (m)
L = fracture length		1	10^{3} (m)
W = fracture width		1	10^{3} (m)

In order to understand the different behavior of CO_2 injection into faults and fractures, it is relevant to point out their differences. Faults are discontinuities of rock units that exhibit a displacement between the two sides of the rupture; in contrast, fractures exhibit no or minimal displacements. Because of the displacements, faults (Fig. 2; cf. Gudmundsson et al., 2002) have a gouge that is formed by the crushing of the rocks during fault slip. The gouge has clastdimensions ranging from breccia to clay-size particles. It frequently has one or more slip planes, which are usually much thinner than the gouge itself and are characterized by finer particles, polished surfaces and striations. In general, both faults (slip planes and fault gouges) and fractures have higher permeabilities than the former contiguous protoliths. In some instances though, the particles of the fault gouge become so small that they evolve to become impermeable barriers. Most faults develop a set of fractures on both sides of them that extend into the unfaulted host rock and constitute the damage zones. Thus, commonly in a fault there are different volumes of rock (specifically the slip-plane, gouge, and damage zone) within the surrounding intact rock. These different volumes have also distinct multiphase fluid flow properties in relation, for instance, to their porosity, pore sizes, pore compressibility, permeability, fracture/fault aperture, degree of offset, etc.

a)

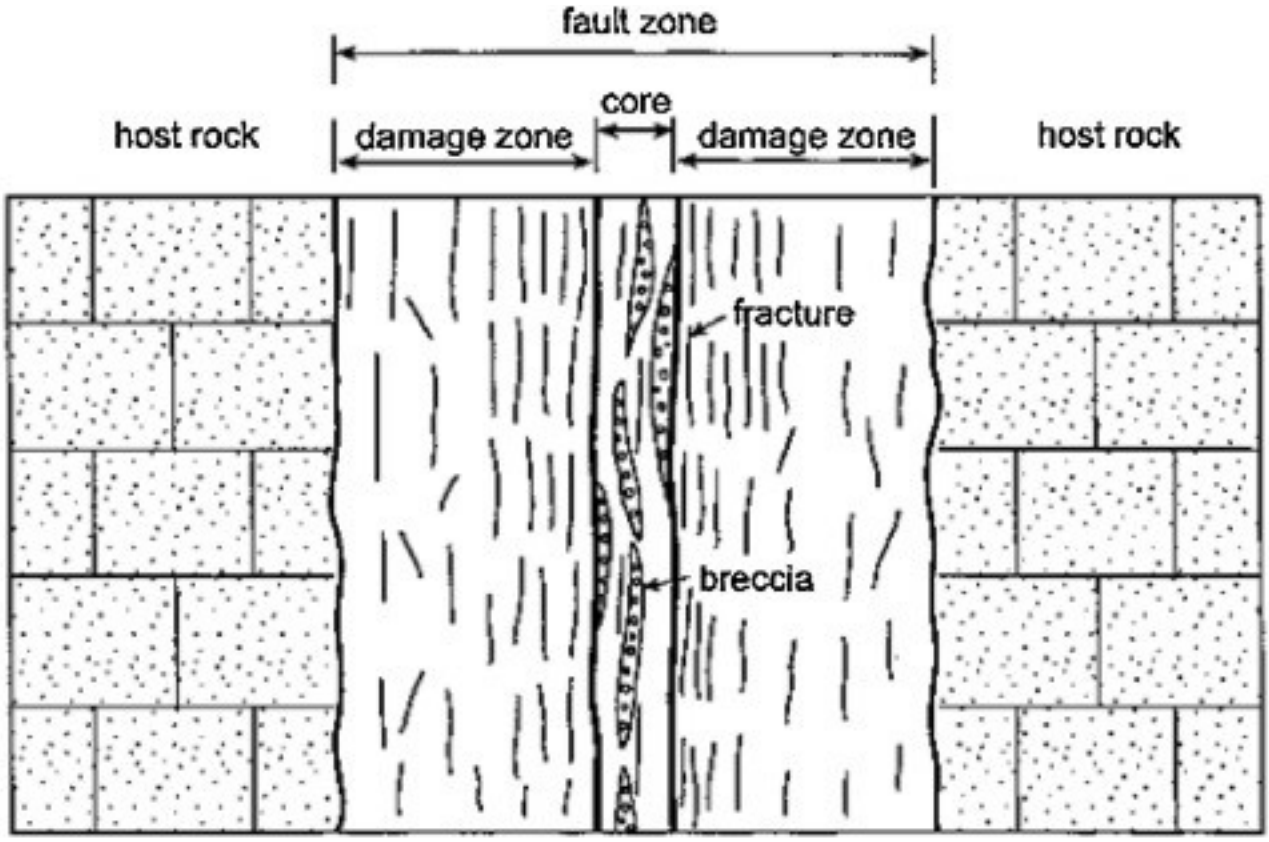
fault zone
core
host rock
damage zone
damage zone
host rock
fracture
breccia

b)

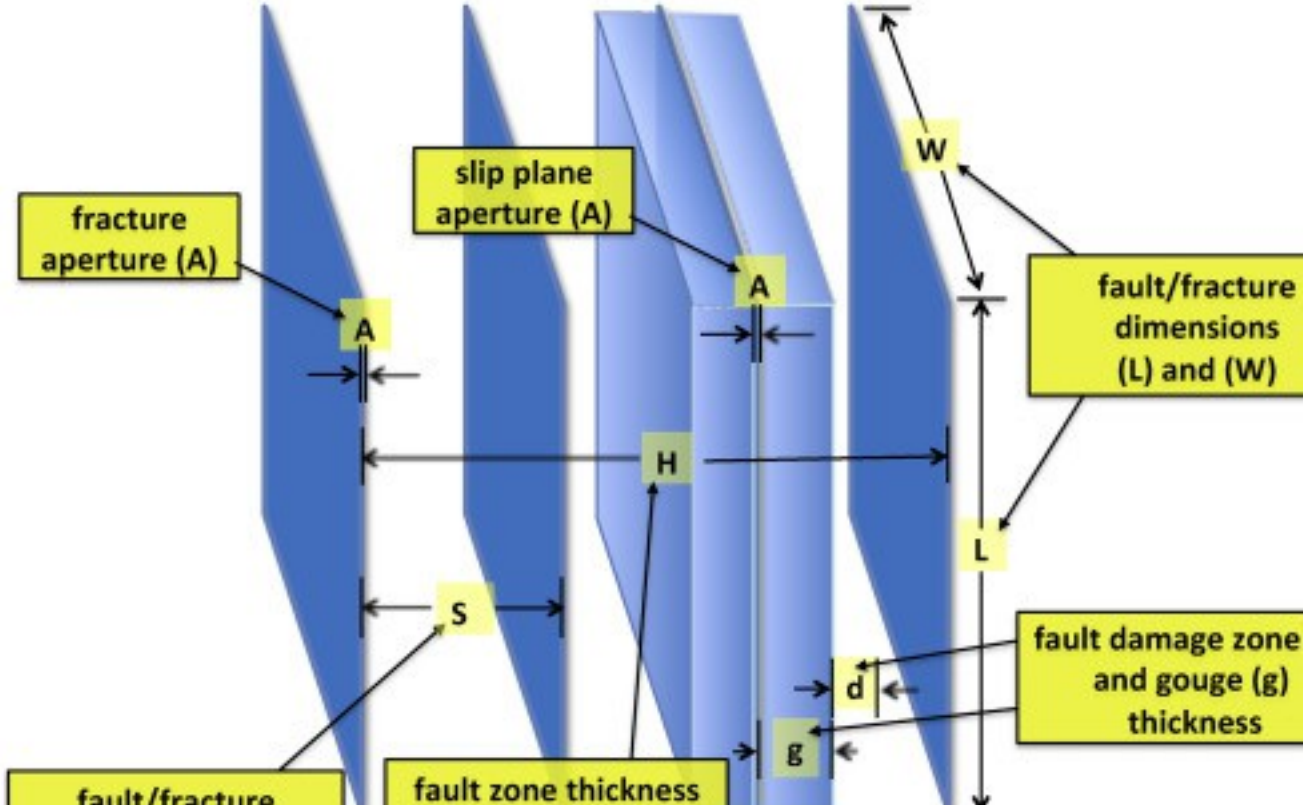
fracture aperture (A)
slip plane aperture (A)
A
A
W
fault/fracture dimensions (L) and (W)
H
L
S
fault damage zone and gouge (g) thickness
d
g
fault zone thickness

1. Download high-res image (895KB)
2. Download full-size image

Fig. 2. a) Conceptual model of fault zone from Gudmundsson et al. (2002), along with b) our schematic model and terminology for a fracture and fault set.

Injecting CO_2 into fractures and faults results in hydrologic and geophysical property changes relative to the initial fully liquid-saturated conditions. Specifically, CO_2 has contrasting wetting properties and very low viscosity relative to hot brine, which promote its flow in the fractures while excluding it from the matrix (Borgia et al., 2012). Therefore, imaging the growth or shrinkage of a CO_2 plume during injection or production tests may give better estimates of the fracture-dominated fluid- and heat-flow parameters. On the geophysical side, CO_2 causes a significant reduction in the stiffness tensor (c_{11}) that in turn results in a reduction in seismic velocity according to the relationship:

(1)$Vp=C11\rho$

Where Vp is the P-wave seismic velocity and ρ is rock density. This observation allows us to use c_{11} as a sensitive indicator of the presence of partially CO_2-saturated fractures or faults, which we will discuss below. Also, the electrical resistivity of brine/CO_2 mixtures varies continuously across the full range of CO_2 saturation (e.g., Nakatsuka et al., 2010). The combination of seismic and other geophysical methods is therefore necessary to push-pull well testing for monitoring the presence of CO_2, and may provide constraints on the fracture/fault network and permeability of the hydrogeologic system.

2.1. Numerical model of injection in a fracture

Fractures in EGSs are mostly vertical, which creates challenges for push-pull testing because the CO_2 tends to rise upward by buoyancy and resists production during the pull cycle. This effect increases with decreasing pressures (depths), because of larger CO_2 compressibility relative to the formation brine. Also, this effect diminishes with decreasing dip of the fracture plane. In practice, in order to image the largest possible section of fractures and faults, this implies that CO_2 must be injected at the greatest feasible depth. By using a simple vertical fracture in our numerical model, we maximize the buoyancy effect of the CO_2 in order to evaluate and address the “buoyancy challenge” in the worst-case configuration.

We model how the CO_2 plume develops during injection and shrinks during production by constructing a 3D vertical fractured volume composed of a single fracture at 1500 m depth (Topology 2 – Fig. 3). We assume that there is no damage zone or matrix adjacent to the fracture. As a first-order approximation, this assumption is reasonable

because supercritical CO_2 will tend to remain in the fracture, being inhibited to enter the matrix due to the brine/CO_2 surface tension (Borgia et al., 2013). This system represents a single independent productive fracture, which is a minimum requirement for a productive geothermal well.

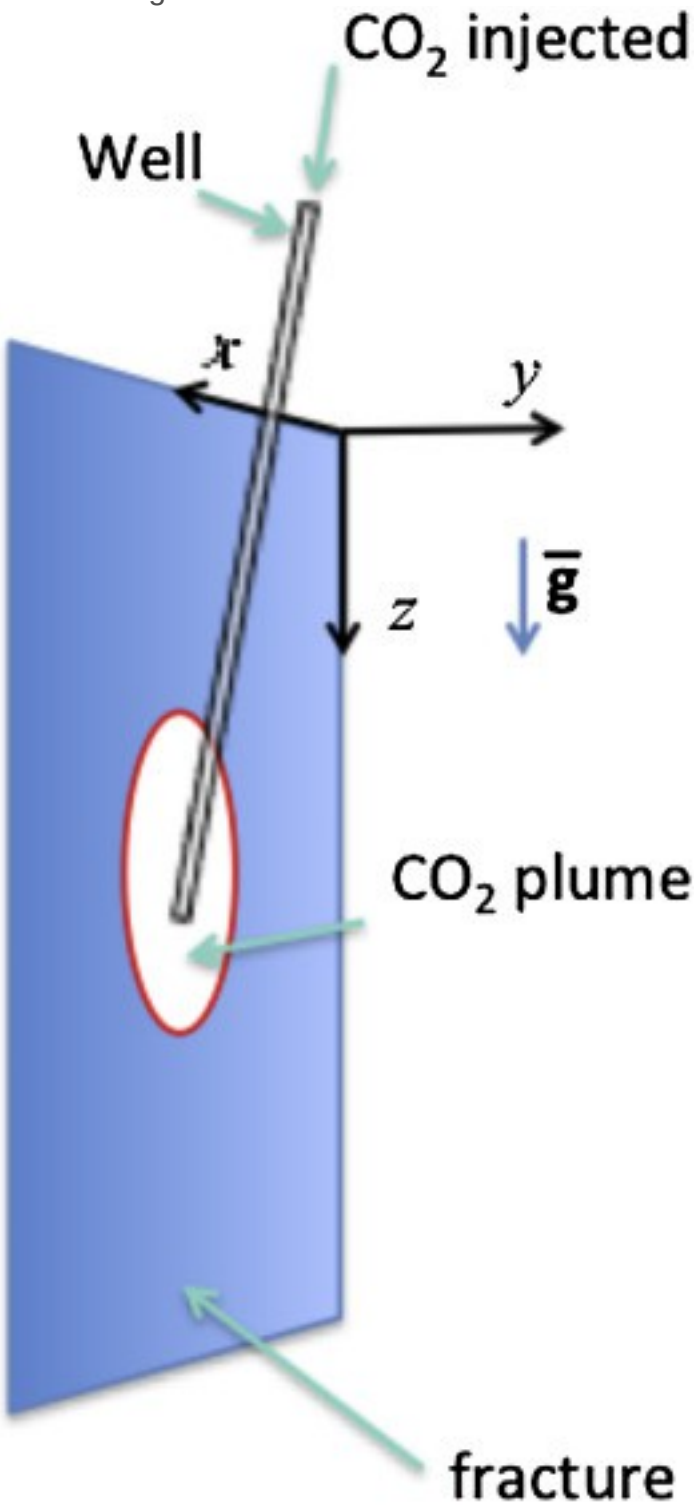

1. Download high-res image (195KB)
2. Download full-size image

Fig. 3. Sketch of the fracture considered in the numerical model (Topology 2) with relevant parameters; the well is excluded from the model.

Our model domain is 500 m by 500 m, respectively in fracture height (L) and width (W), and 10^{-4} m perpendicular to the fracture. This model corresponds to Topology 2 with the gravity vector in the z-direction parallel to the fracture (cf. Fig. 1). Grid cells are 5×5 m^2 along the fracture plane. The boundary conditions are varied from those representing a lateral (top and bottom) unconfined fracture, to a poorly confined and, finally, to a fully confined fracture according to which fracture boundaries are assumed to be closed. We are not considering the presence of different fracture sets, thus the fracture, even if unconfined, remains unconnected to other fractures.

We model non-isothermal, two-phase flow with TOUGH2 V2.0 (Pruess et al., 2012) using the equation-of-state module ECO2N (Pan et al., 2016). We include the effects created by capillary pressure, and salt precipitation and dissolution with, respectively, the associated permeability reduction and increase.

We inject CO_2 at 20 °C, with a constant overpressure of 2 MPa relative to hydrostatic (see Table 2, Table 3 for relevant parameters), for a period of 10 days. During the subsequent 10-day production test we recover fluids against a constant depressurization of −4 MPa relative to hydrostatic. Effective production needs a larger pressure difference to minimize the effect of CO_2buoyancy, thus allowing a higher CO_2 recovery. Our experiments also include tests for injection and production with different permeabilities (10^{-12}–10^{-13} m^2), and constant injection/production flow rates (100–500 kg/s).

Table 2. Conditions for push-pull experiments in a fracture.

Initial conditions
Pressure = hydrostatic;
NaCl mass fraction in the aqueous solution = 0.10;
CO_2 mass fraction in the aqueous solution = $1.0 * 10^{-6}$;
Temperature = 200 °C.
Injection run
Pressure = $20 * 10^5$ Pa above hydrostatic in the injection element;
CO_2 mass fraction in the gas phase of the injection element = 0.99;
Temperature = 20 °C in the injection element.
Production run

Initial conditions are equal to those at the end of the injection period.

Pressure = 40 *10^5 Pa below hydrostatic in the production element.

Table 3. Model parameters for push-pull simulations.

Parameter	Units	Fracture	Fault slip plane	fault gouge	damage zone	matrix
thickness	m	10^{-4}	10^{-4}	1	5	10
porosity	volume fraction	0.2	0.5	0.1	0.05	0.01
permeability	m^2	10^{-12}–10^{-13}	10^{-12}–10^{-13}	10^{-13}	10^{-14}	10^{-16}
rock grain density	kg/m^3	2650	2650	2650	2650	2650
rock grain specific heat	J/(kg K)	1000	1000	1000	1000	1000
thermal conductivity[a]	W/(m K)	2.1	2.1	2.1	2.1	2.1
Klinkenberg parameter	Pa^{-1}	7.6×10^{-5}	7.6×10^{-5}	7.6×10^{-5}	7.6×10^{-5}	7.6×10^{-5}
capillary pressure VanGenuchten[b]	Pa	none	none	$\lambda = 0.4438$; $S_{lr} = 0.0$, $1/P_0 = 2.402e{-}4$ Pa^{-1}; $P_{max} = 1.0e8$ Pa; $S_{ls} = 1.0$;	$\lambda = 0.4438$; $S_{lr} = 0.0$, $1/P_0 = 1.485e{-}6$ Pa^{-1}; $P_{max} = 1.0e8$ Pa; $S_{ls} = 1.0$;	$\lambda = 0.4438$; $S_{lr} = 0.0$, $1/P_0 = 1.485e{-}6$ Pa^{-1}; $P_{max} = 1.0e8$ Pa; $S_{ls} = 1.0$;
relative permeability Corey[c]		$S_{lr} = 0.3$; $S_{gr} = 0.05$;	$S_{lr} = 0.3$; $S_{gr} = 0.05$;	$S_{lr} = 0.3$; $S_{gr} = 0.05$;	$S_{lr} = 0.3$; $S_{gr} = 0.05$;	$S_{lr} = 0.3$; $S_{gr} = 0.05$;

a

Under liquid-saturated conditions.

b

Van Genuchten (1980).

c

Corey (1954).

For the applied injection pressure (or flow rate), a high pressure gradient forms around the well, which extends outward, decreasing in magnitude as the CO_2plume develops (Fig. 4). During production the high pressure gradient moves back toward the well. The CO_2 penetrates most of the fracture, pushing the gas-brine interface away from the well (Fig. 5).

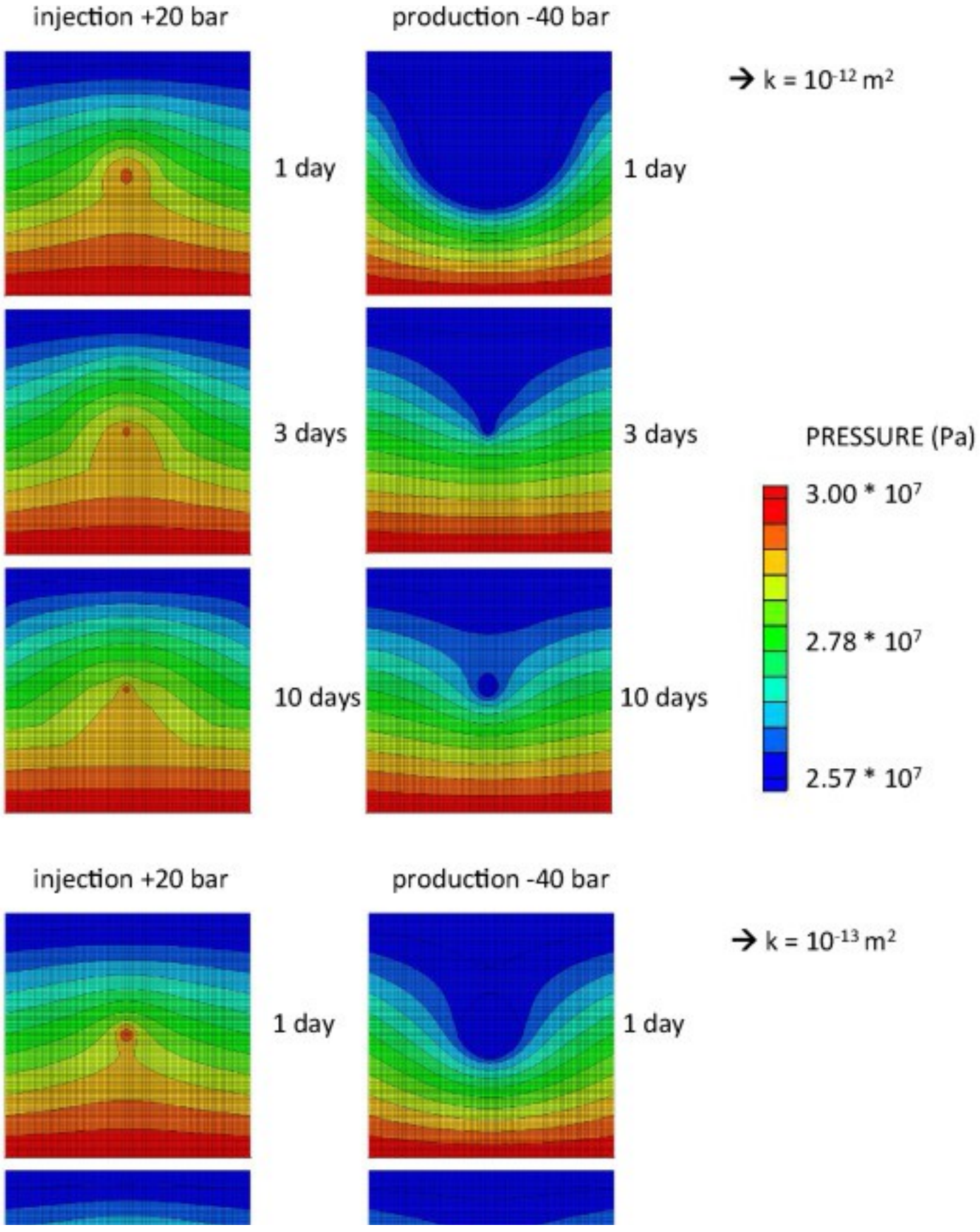
injection +20 bar
production -40 bar
→ k = 10-12 m2
1 day
1 day
3 days
3 days
10 days
10 days
PRESSURE (Pa)
3.00 * 107
2.78 * 107
2.57 * 107
injection +20 bar
production -40 bar
→ k = 10-13 m2
1 day
1 day

1. Download high-res image (3MB)
2. Download full-size image

Fig. 4. Numerical results: pressure variations during injection and production in the fracture elements. a) Note the large pressure anomaly developing at the start of injection, which decreases as injection continues, then reverses as the CO_2 is pumped back into the well. b) For lower permeabilities this pressure anomaly becomes smaller for equal times both during injection and production. Note that for an order of magnitude decrease in permeability there is an order of magnitude increase in time to reach a similar pressure anomaly.

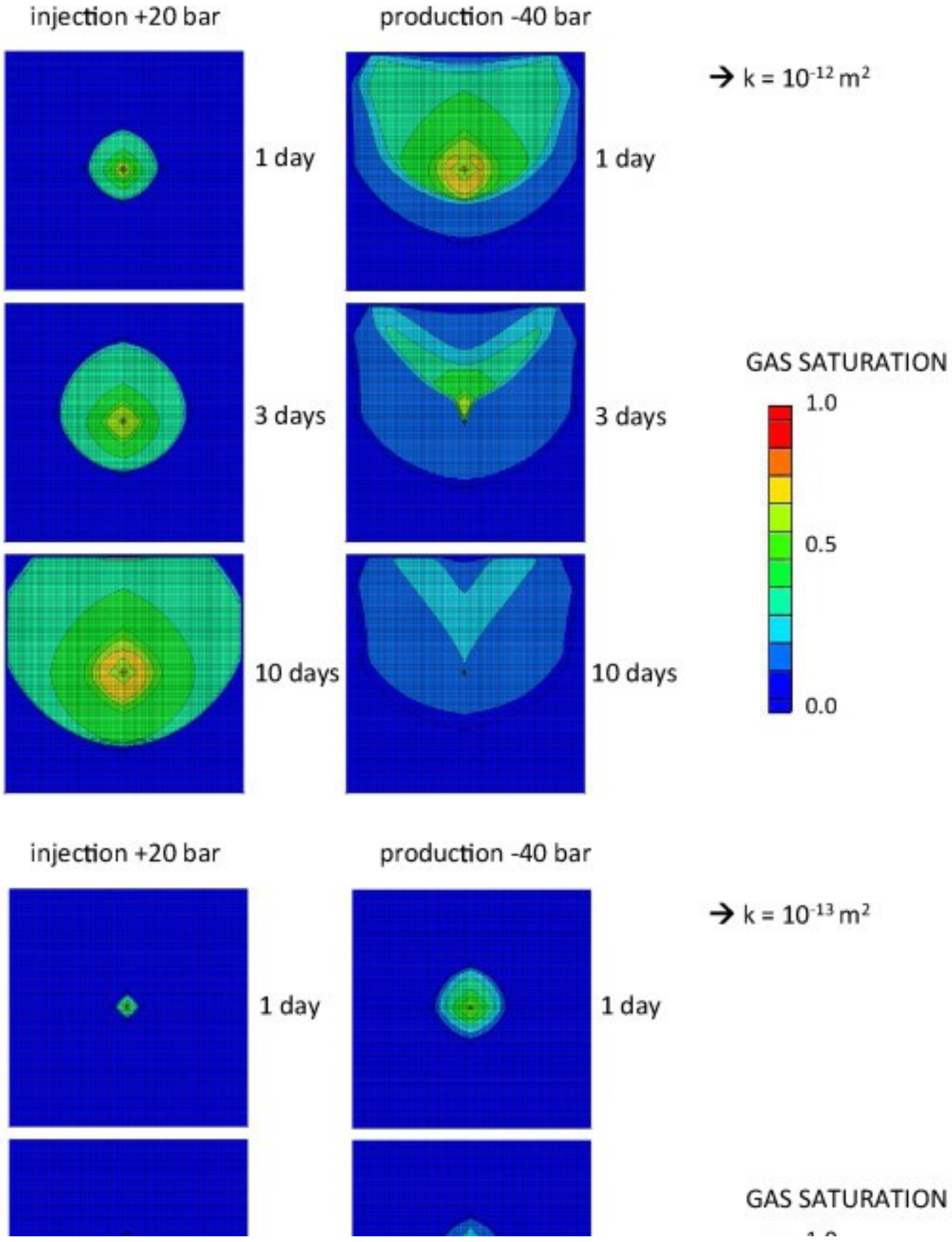
injection +20 bar
production -40 bar
→ k = 10-12 m2
1 day
1 day
3 days
3 days
10 days
10 days
GAS SATURATION
1.0
0.5
0.0
injection +20 bar
production -40 bar
→ k = 10-13 m2
1 day
1 day
GAS SATURATION

1. Download high-res image (2MB)
2. Download full-size image

Fig. 5. Numerical results: CO_2 saturation during injection and production in the fracture elements. a) For a higher permeability a larger CO_2 saturation anomaly is created that reaches the model top and lateral boundaries. Buoyancy effects become particularly relevant during production. b) For an order of magnitude lower permeability, a proportionally smaller plume develops at equal times, and buoyancy flow is much less significant. Note that after 10 days of production much, but not all, CO_2 is recovered, the pores volume being still occupied by 10–20% gas.

While close to the well the gas saturation becomes 100% almost immediately, the overall plume has an average gas saturation of 30–60%. This allows for a remarkably good filling of the fracture and optimal potential for fracture characterization (e.g., using time-lapse seismic) given the contrast in fluid properties both in space and time. Also, the buoyancy effects of the plume are limited, but become more important during the following production test. Buoyancy is larger for higher permeability and longer injection times. A small amount of salt precipitates as the CO_2 gas plume dries out the fracture, but tends to re-dissolve into the brine during the following production test as the brine reenters the fracture. The thermal component during the process of CO_2plume development are negligible.

The system behaves quite differently during injection and production. While the CO_2-plume grows approximately symmetrically during injection, because of buoyancy, the plume does not shrink symmetrically during production, inhibiting the recovery of CO_2: about 10–20% of the volume of the fracture still remains filled with CO_2 (Fig. 5). In natural conditions, we expect that the recovery of CO_2 during production will be even more limited due to capillary trapping of the CO_2 as soon as the gas phase loses hydraulic continuity between adjacent pores. In the simulations with higher fracture permeability (10^{-12} m^2 relative to 10^{-13} m^2), a proportionally larger CO_2 plume develops (Fig. 4, Fig. 5), making the CO_2-push-pull experiment very effective as the basis for estimating fracture porosity and permeability.

Fig. 6 shows the supercritical gas-phase (CO_2 + H_2O) density distribution in the fracture during the experiment. Because of high compressibility of this gas, a density stratification forms in the fracture, which enhances buoyancy. During production the density and the density gradient of the supercritical gas decreases through the fracture. As for the other physical parameters, for smaller permeabilities the density anomaly forms proportionally later.

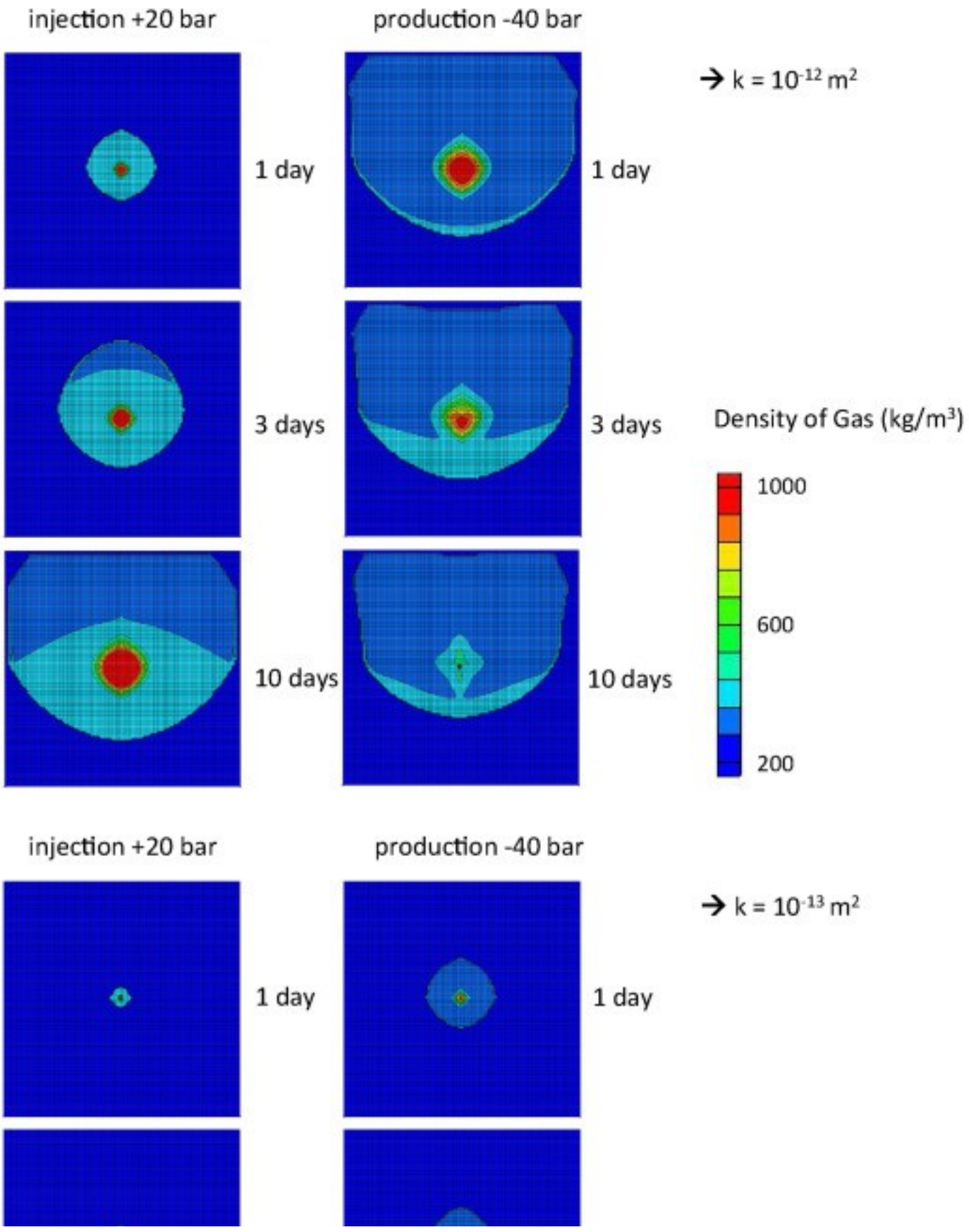
injection +20 bar
production -40 bar
→ k = 10-12 m2
1 day
1 day
3 days
3 days
10 days
10 days
Density of Gas (kg/m3)
1000
600
200
injection +20 bar
production -40 bar
→ k = 10-13 m2
1 day
1 day

1. Download high-res image (2MB)
2. Download full-size image

Fig. 6. Numerical results: gas phase density during injection and production in the fracture elements. a) For a larger permeability, a measurable density stratification forms in the fracture that enhances the buoyancy effect. However, buoyancy becomes particularly relevant only during production. During this phase of the experiment the density, as well as the density gradient, of the gas decreases all through. b) For smaller permeabilities the density anomaly forms proportionally later.

3. Numerical model of injection in a fault

Simulations of the push-pull injection-production of CO_2 in a fault is carried out using the model's domain dimensions and the symmetry, which allows us to model only one-quarter of the full system in order to reduce the number of elements and consequently the calculation time. The system is shown in Fig. 7(Oldenburg et al., 2016). We use a discretization with grid blocks of size 20 m × y × 20 m, where $y = 10^{-4}$ m in the slip-plane, and 10^{-3}, 10^{-2}, 10^{-1}, and ∼1 m in the fault gouge, 10^{-1} m in the damage zone, and ∼1 m, and ∼10 m in the matrix. The fault is assumed to have between 2 and 3 km depth, with a geothermal gradient of 40 °C/km, fully saturated by a brine with salt mass fraction equal to 0.1, and at hydrostatic pressure. The boundary condition is closed to fluid flow on the top and open to fluid flow on the sides and bottom. Material properties used in the model are given in Table 3. Results of the preliminary simulations showing pressure and CO_2 saturation are shown in Fig. 8 for ten days of injection (push) with 2 MPa overpressure, and one day of production (pull) with 4 MPa underpressure relative to the initial hydrostatic pressure.

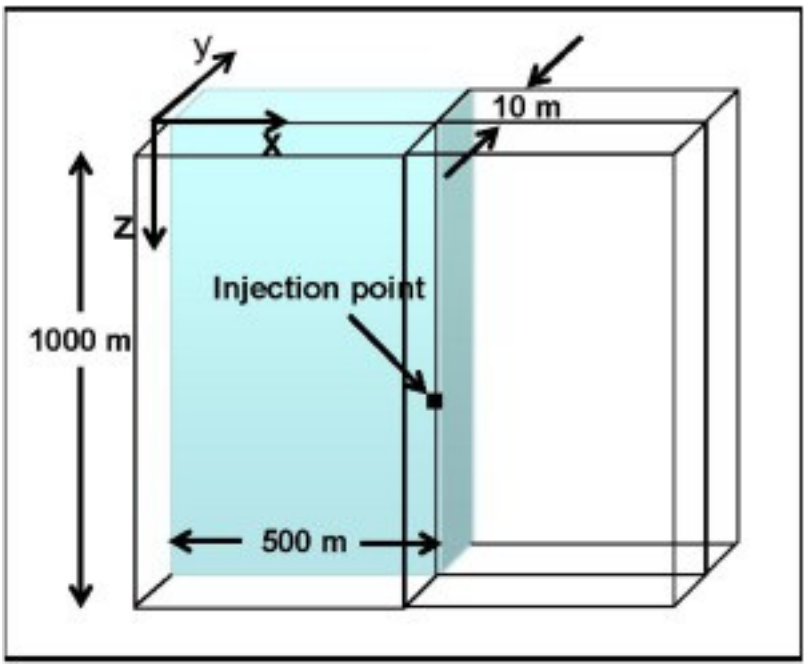

1. Download high-res image (153KB)
2. Download full-size image

Fig. 7. Model domain for the push-pull simulations. Because of symmetry, we only model one-quarter of the actual system.

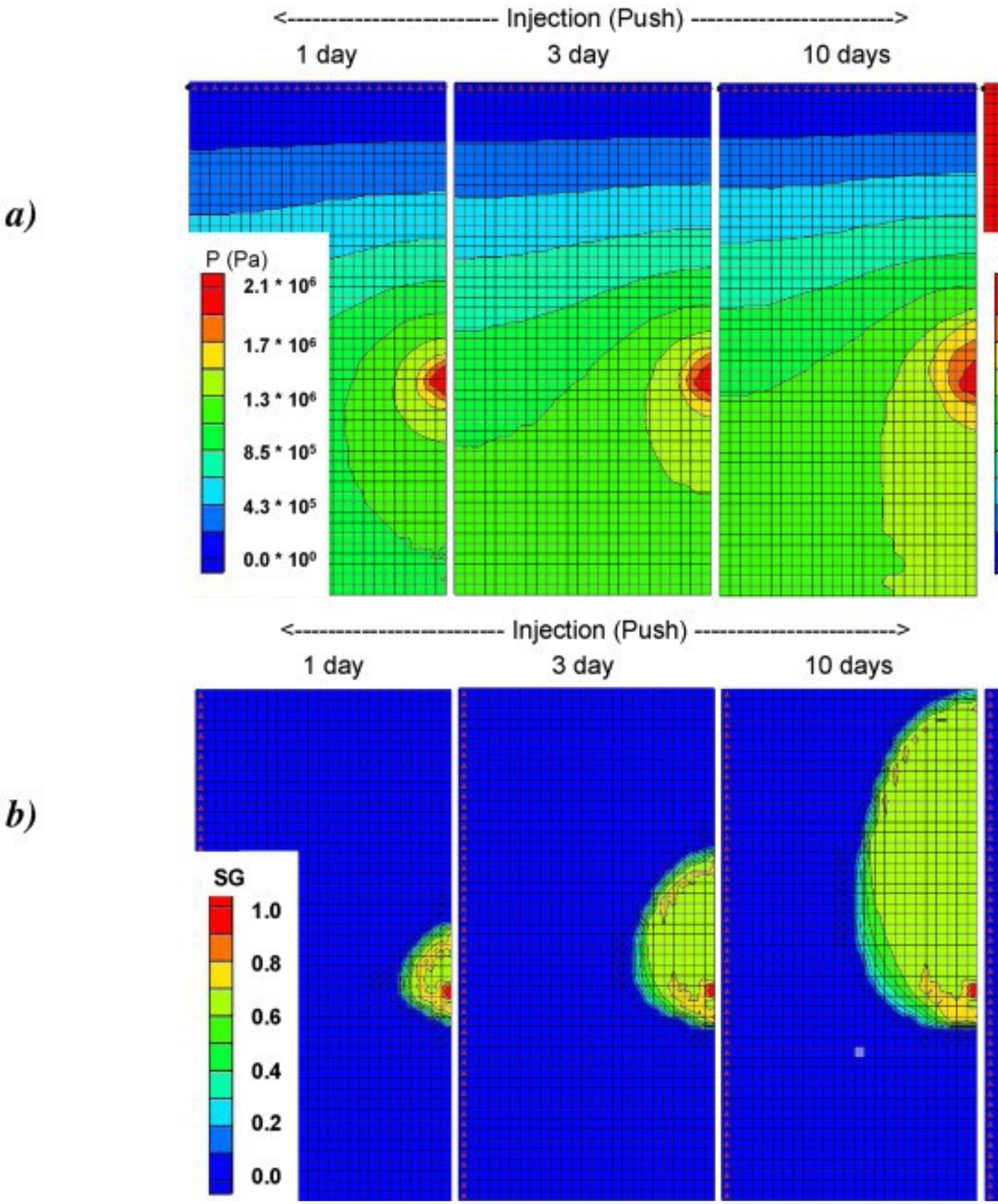
a)
<---------- Injection (Push) ---------->
1 day
3 day
10 days
P (Pa)
2.1 * 10^6
1.7 * 10^6
1.3 * 10^6
8.5 * 10^5
4.3 * 10^5
0.0 * 10^0
b)
<---------- Injection (Push) ---------->
1 day
3 day
10 days
SG
1.0
0.8
0.6
0.4
0.2
0.0

1. Download high-res image (4MB)
2. Download full-size image

Fig. 8. a) Pressure distribution in the slip plane for the closed top boundary case; b) CO_2saturation in the slip plane showing buoyant rise of CO_2. Buoyancy makes it difficult to produce the CO_2 back during the pull phase; c) CO_2 saturation in the gouge showing smaller saturation than in the slip plane but still significant for property contrast especially considering the larger thickness of the gouge relative to the slip plane.

As shown in Fig. 8a, at the beginning of the push experiment a large pressure gradient develops in the system that becomes smaller with time. A large CO_2plume forms and moves upward because of buoyancy (Fig. 8b). Relative to the previous simulation with initial constant temperature; i.e., there is no geothermal gradient; Fig. 4, Fig. 5, Fig. 6) in this simulation the CO_2 buoyancy is enhanced by the geothermal gradient, because the hotter, less dense CO_2continuously moves upward into lower temperature, higher density brine, resulting in an extended upward plume. Therefore, it is harder to produce back the CO_2 during the pull phase, which after less than one day evolves to a stead-state production of brine only.

The fact that during the push-phase of the simulation practically pure supercritical CO_2 is injected, while during the pull-phase mainly brine is produced (that is, two fluids with substantially different physical properties) results in an additional mean for a more accurate characterization of the fault system. Fig. 8c shows the CO_2 saturation in the gouge, which forms a smaller plume with lower saturation. This plume, however, is thicker than that in the slip plane and therefore potentially creates a larger contrast for geophysical detection.

4. preliminary modeling of geophysical response

The above CO_2 injection and production simulation results can be used for preliminary modeling of the geophysical imaging of fractures and faults, which would improve characterization of EGS sites. A complete description of geophysical modeling results will be presented in a future paper. Here we report only on the actual feasibility of seismically detecting the CO_2-filled fracture or fault. Seismic response is sensitive to subsurface fluid properties because different fluids can lead to distinguishable elastic properties of the rock-fluid system (Batzle and Wang, 1992). By using a fracture/rock physics model (Nakagawa and Schoenberg, 2007), we have made preliminary estimates of how the four elements of the stiffness tensor vary with CO_2saturation as shown in Fig. 9. C_{11} is the normal stiffness in the horizontal direction perpendicular to the fracture plane; C_{22} is the normal stiffness in the vertical direction parallel to the fracture

plane; C_{33} is the shear modulus; and C_{12} is the transitional stiffness. We find that across the CO_2 saturation range, C_{11} varies by about 15%. It reaches a maximum between 0% and 10%, then decreases exponentially with increasing saturations (Fig. 9).

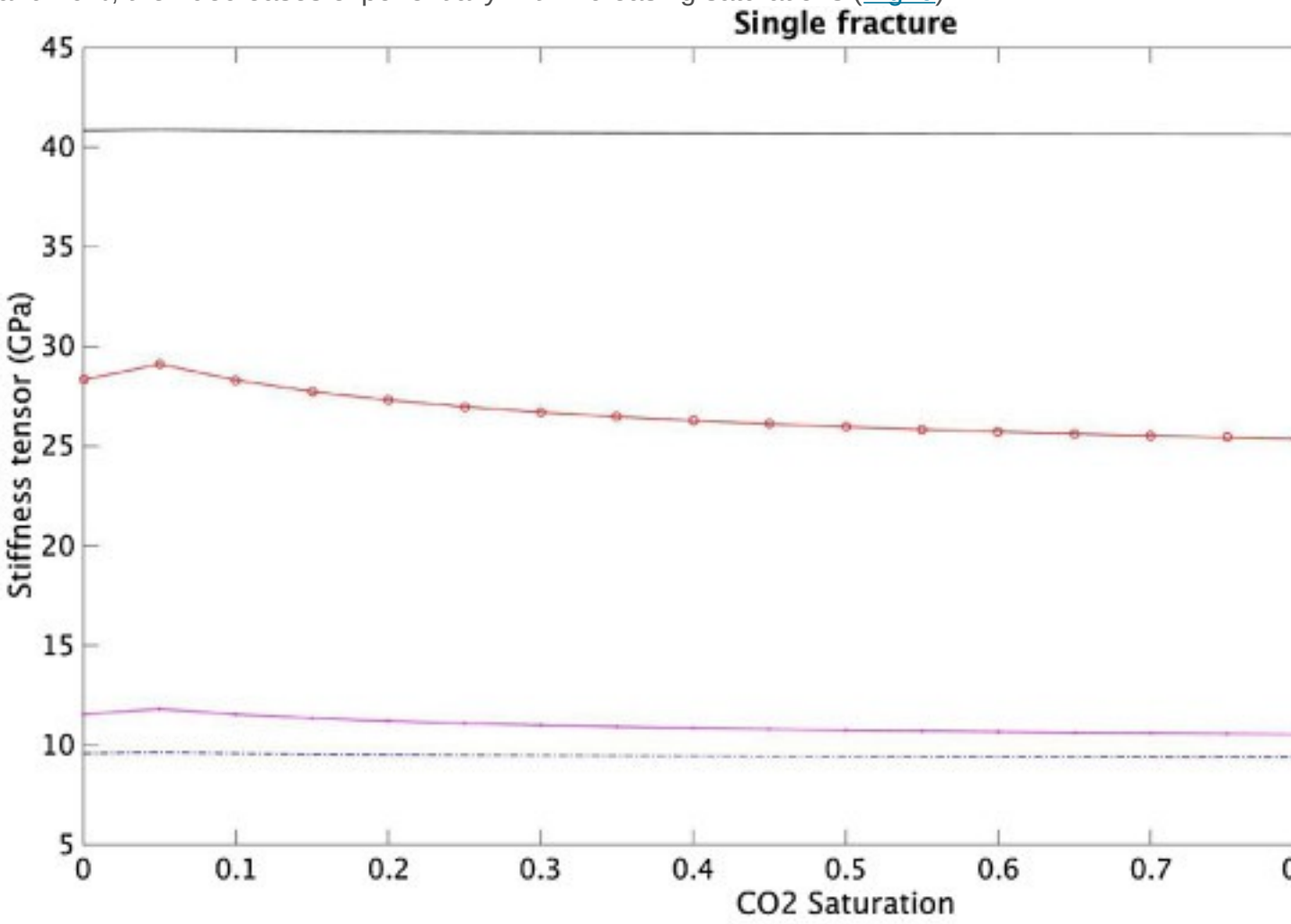

1. Download high-res image (296KB)
2. Download full-size image

Fig. 9. Stiffness tensor elements as a function of CO_2 saturation.

The geometry of the seismic model for fracture zone detection is shown in Fig. 10a and the simulated horizontal component of the surface seismic records are shown in Fig. 10b. This simulation shows a measurable difference at CO_2saturations between 0% and 50% even with a 10% random noise added to the records, which is done to mimic real field situation.

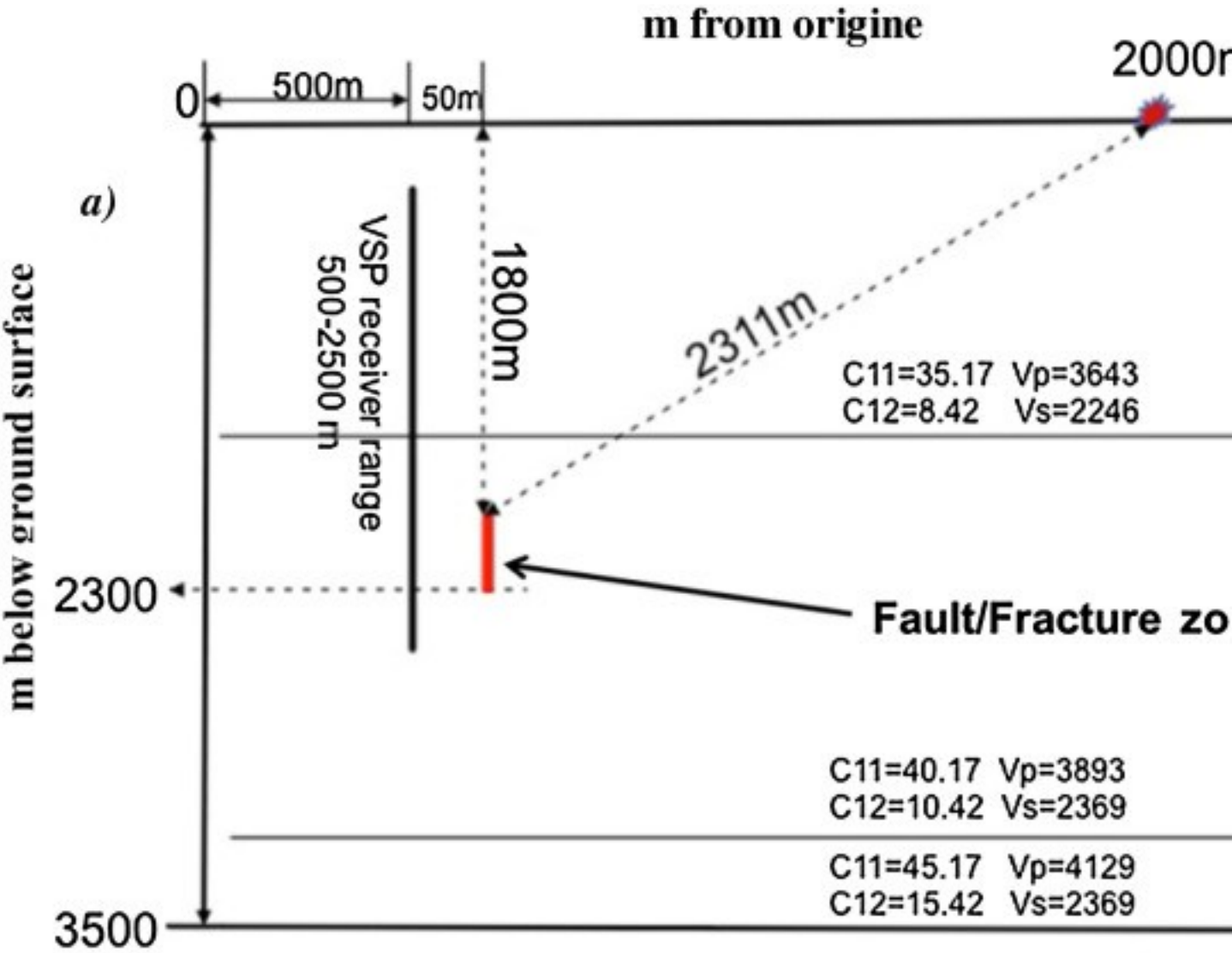
m from origine
2000r
0
500m
50m
a)
VSP receiver range
500-2500 m
1800m
2311m
C11=35.17 Vp=3643
C12=8.42 Vs=2246
m below ground surface
2300
Fault/Fracture zo
C11=40.17 Vp=3893
C12=10.42 Vs=2369
C11=45.17 Vp=4129
C12=15.42 Vs=2369
3500

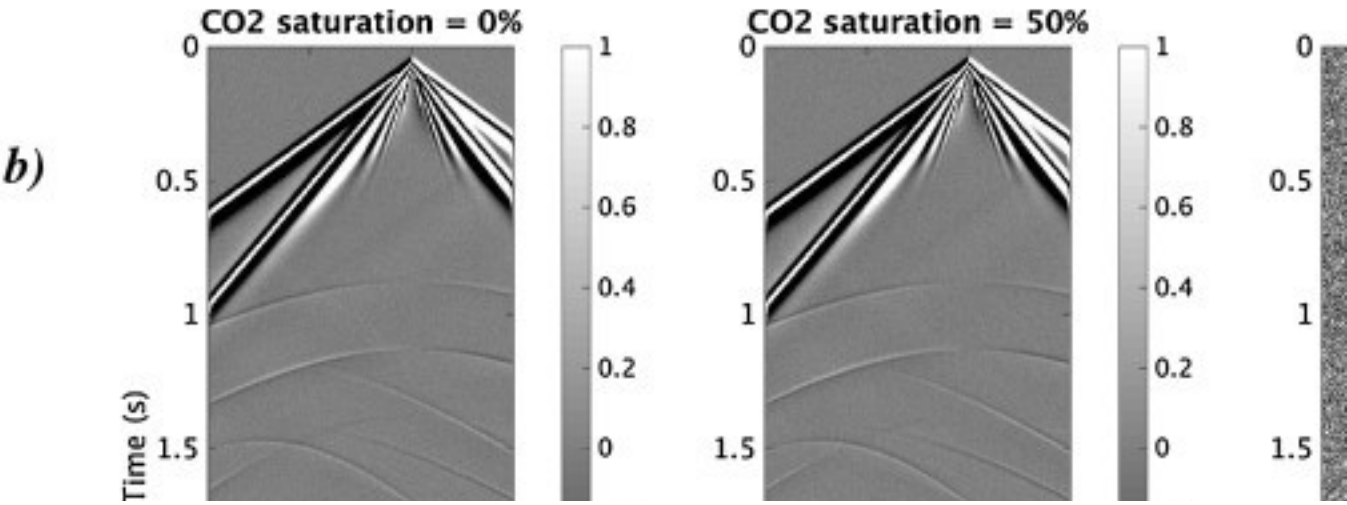
b)
CO2 saturation = 0%
CO2 saturation = 50%
Time (s)
0
0.5
1
1.5
0.8
0.6
0.4
0.2

1. Download high-res image (1MB)
2. Download full-size image

Fig. 10. Preliminary seismic imaging of a CO_2-filled fracture/fault (after Oldenburg et al., 2016). a) The conceptual model for simulating active seismic imaging of a fault zone (red), which consists of ten 500 m-high fracture planes that are spaced 1 m apart − this is the geophysical equivalent of a 10 m wide fault gouge −. Anisotropic elastic constants (GPa) and isotropic background velocities (m/s) are shown for each layer. The seismic source is 2000 m away from the fault; b) Horizontal component of the surface seismic response showing an identifiable difference between 0% and 50% CO_2 saturation, even with an added 10% noise.

These promising results are preliminary and are subject to refinement. We are carrying out research to fully integrate the modeling of CO_2 push-pull simulations with active seismic, well-logging, and pressure transient monitoring approaches to evaluate the potential of this integrated CO_2-injection-based approach to improve stimulation design and implementation specifically, and EGS site characterization in general.

5. Conclusions

In our numerical experiments we find that, for a 2 MPa overpressure during injection, buoyancy influences the flow of the injected CO_2 even during short injection periods. This effect becomes higher for larger geothermal gradients, permeabilities, and longer injection times.

There is a strong difference between injection and production. While the CO_2plume tends to grow sideward and upward during injection, mainly because of buoyancy and capillary trapping, not all CO_2 is recovered during the production phase. In the case where the most CO_2 is recovered, at least 10% of the volume of the pores still remains filled with capillary trapped CO_2.

In the experiments with higher rock permeability (10^{-12} m^2 relative to 10^{-13} m^2), a significantly larger CO_2 plume is developed, making the CO_2-push-pull experiment at constant pressure very effective in measuring permeability. Thermal influence is insignificant during the injection period because porosity is small and the heat content of the rock mass is much larger than that of the mass of the injected CO_2. For the same reason there is practically no change in the temperature field during production.

Depending on the modeled seismic and geophysical logging contrasts arising from the CO_2 in the fracture, more effective fracture characterization may be possible at EGS sites. The geophysical modeling suggests a measurable change in the elastic moduli (stiffness tensor), related to CO_2 displacing the brine in a fracture or fault. The moduli change depends on the component of the stiffness tensor being considered. This

variability can be used to optimize the design of the geometry of the seismic data acquisition system to monitor the CO_2 injection/production experiments.

Acknowledgments

Support for this work was provided by the Office of Energy Efficiency and Renewable Energy, Geothermal Technologies Office, U.S. Department of Energy. Additional support was provided by the Assistant Secretary for Fossil Energy (DOE), Office of Coal and Power Systems, through the National Energy Technology Laboratory (NETL), and by Lawrence Berkeley National Laboratory under Department of Energy Contract No. DE-AC02-05CH11231. Financial support was also provided by EDRA to A. Borgia. TOUGH2 grid generation and data visualization was done using a GMS™ license provided by Aquaveo.

References

Batzle and Wang, 1992

M. Batzle, Z. Wang**Seismic properties of pore fluid**
Geophysics, 57 (11) (1992), pp. 1396-1408
CrossRefView Record in Scopus

Borgia et al., 2012

A. Borgia, K. Pruess, T.J. Kneafsey, C.M. Oldenburg, L. Pan**Numerical simulation of salt precipitation in a fractured CO2-Enhanced geothermal system**
Geothermics, 44 (2012), pp. 13-22, 10.1016/j.geothermics.2012.06.002
ArticleDownload PDFView Record in Scopus

Borgia et al., 2013

A. Borgia, K. Pruess, T.J. Kneafsey, C.M. Oldenburg, L. Pan**Simulation of CO_2-EGS in a fractured reservoir with salt precipitation**
Energy Procedia, 37 (2013), pp. 6617-6624, 10.1016/j.egypro.2013.06.594
ArticleDownload PDFView Record in Scopus

Borgia et al., 2015

A. Borgia, C.M. Oldenburg, R. Zhang, L. Pan, S. Finsterle, T.S.Ramakrishnan**Simulations of CO_2 push-pull in fractures to enhance geophysical contrast for characterizing EGS sites**
PROCEEDINGS, TOUGH Symposium 2015, Lawrence Berkeley National Laboratory, Berkeley, California, September 28–30 (2015), pp. 109-115
View Record in Scopus

Corey, 1954

A.T. Corey**The interrelation between gas and oil relative permeabilities**
Producers Mon., 19 (1) (1954), pp. 8-41

Genter et al., 2010

A. Genter, K. Evans, N. Cuenot, D. Fritsch, B. Sanjuan**Contribution of the exploration of deep crystalline fractured reservoir of Soultz to the knowledge of enhanced geothermal systems (EGS)**
C.R. Geosci., 342 (7) (2010), pp. 502-516
ArticleDownload PDFView Record in Scopus

Gudmundsson et al., 2002

A. Gudmundsson, I. Fjeldskaar, S.L. Brenner**Propagation pathways and fluid transport of hydrofractures in jointed and layered rocks in geothermal fields**
J. Volcanol. Geotherm. Res., 116 (3) (2002), pp. 257-278
ArticleDownload PDFView Record in Scopus

Nakagawa and Schoenberg, 2007

S. Nakagawa, M. Schoenberg**Poroelastic modeling of seismic boundary conditions across a fracture**
J. Acoust. Soc. Am. (2007)

Nakatsuka et al., 2010

Y. Nakatsuka, Z. Xue, H. Garcia, T. Matsuoka**Experimental study on CO_2 monitoring and quantification of stored CO_2 in saline formations using resistivity measurements**
Int. J. Greenh. Gas Control, 4 (2010), pp. 209-216
ArticleDownload PDFView Record in Scopus

Oldenburg et al., 2016

C.M. Oldenburg, T.M. Daley, A. Borgia, R. Zhang, C. Doughty, T.S.Ramakrishnan, B. Altundas, N. Chugunov**Preliminary simulations of carbon dioxide injection and geophysical monitoring to improve imaging and characterization of faults and fractures at EGS sites**
Proc. 41st Workshop Ib Geothermal Reservoir Engineering, Stanford University, Stanford, CA, February 22–24 (2016)
(9 pp.)

Pan et al., 2016

L. Pan, N. Spycher, C. Doughty, K. Pruess**ECO2N V2.0: A TOUGH2 fluid property module for modeling CO_2-H_2O-NaCL systems to elevated temperatures of up to 300 °C**
Greenhouse Gases Sci. Technol. (2016), 10.1002/ghg.1617

Pruess et al., 2012

K. Pruess, C. Oldenburg, G. Moridis**TOUGH2 User's Guide, Version 2.0, Report LBNL-43134 (revised)**
Lawrence Berkeley National Laboratory, Berkeley, California (2012)

Van Genuchten, 1980

M.T. Van Genuchten**A closed-form equation for predicting the hydraulic conductivity of unsaturated soils**

Soil Sci. Soc. Am. J., 44 (5) (1980), pp. 892-898

CrossRefView Record in Scopus

		Fracture	Fault			
·	Units		slip plane	fault gouge	damage zone	matrix
	m	10^{-4}	10^{-4}	1	5	10
	volume fraction	0.2	0.5	0.1	0.05	0.01
:y	m^2	10^{-12}–10^{-13}	10^{-12}–10^{-13}	10^{-13}	10^{-14}	10^{-16}
	kg/m^3	2650	2650	2650	2650	2650
at	J/(kg K)	1000	1000	1000	1000	1000
y[a]	W/(m K)	2.1	2.1	2.1	2.1	2.1
g	Pa^{-1}	7.6×10^{-5}	7.6×10^{-5}	7.6×10^{-5}	7.6×10^{-5}	7.6×10^{-5}
hten[b]	Pa	none	none	λ = 0.4438; S_{lr} = 0.0, $1/P_0$ = 2.402e–4 Pa^{-1}; P_{max} = 1.0e8 Pa; S_{ls} = 1.0;	λ = 0.4438; S_{lr} = 0.0, $1/P_0$ = 1.485e–6 Pa^{-1}; P_{max} = 1.0e8 Pa; S_{ls} = 1.0;	λ = 0.4438; S_{lr} = 0.0, $1/P_0$ = 1.485e- 6 Pa^{-1}; P_{max} = 1.0e8 P S_{ls} = 1.0;
		S_{lr} = 0.3;	S_{lr} = 0.3;	S_{lr} = 0.3;	S_{lr} = 0.3;	S_{lr} = 0.3;